

## MAGNETIC HELICITY INJECTION BY HORIZONTAL FLOWS IN THE QUIET SUN. I. MUTUAL-HELICITY FLUX

B. T. WELSCH<sup>1</sup>

Space Sciences Laboratory, University of California, Berkeley, CA 94720-7450; welsch@ssl.berkeley.edu

AND

D. W. LONGCOPE

Physics Department, Montana State University, Bozeman, MT 59717-3840; dana@physics.montana.edu

Received 2002 May 10; accepted 2003 January 9

### ABSTRACT

The flux of magnetic helicity through the solar photosphere has implications in diverse areas of current solar research, including solar dynamo modeling and coronal heating. In this work, we focus on the flux of magnetic helicity from quiet-Sun magnetic fields. We express the total helicity flux in terms of mutual and self-helicities, which arise from relative motions of separate flux elements and from internal motions within individual magnetic flux elements, respectively. Using a novel labeling algorithm and a tracking algorithm applied to high-cadence, high-resolution *Solar and Heliospheric Observatory* Michelson Doppler Imager magnetograms, we determine the observed mutual-helicity flux density in the quiet Sun to be  $\sim 5 \times 10^{12} \text{ Mx}^2 \text{ cm}^{-2} \text{ s}^{-1}$  and compare this value with a simple theoretical prediction. The observed rate corresponds to a whole-cycle, hemispheric mutual-helicity flux of  $\sim 10^{43} \text{ Mx}^2$  from the quiet Sun, meaning that helicity injection by surface motions in quiet-Sun fields is negligible compared to the active region helicity flux rate.

*Subject headings:* MHD — Sun: magnetic fields

### 1. INTRODUCTION

Magnetic helicity has been widely recognized as a useful tool in the study of solar magnetic fields (see, e.g., Rust’s 2002 review and references therein). Within a finite volume  $V$ , whose boundary is not a flux surface, the term “helicity” generally refers to the gauge-invariant relative helicity (Berger & Field 1984). The relative helicity can be expressed as the integral (Finn & Antonsen 1985)

$$\mathcal{H} = \int_V d^3x (\mathbf{A} + \mathbf{A}_P) \cdot (\mathbf{B} - \mathbf{B}_P), \quad (1)$$

where  $\mathbf{B}_P$  is the unique potential magnetic field matching the normal component of actual field  $\mathbf{B}$  at the boundary and  $\mathbf{A}$  and  $\mathbf{A}_P$  are vector potentials generating  $\mathbf{B}$  and  $\mathbf{B}_P$ , respectively. The relative helicity is defined to be zero for a potential field.

Within a highly conducting plasma, the relative helicity is approximately conserved (Taylor 1974) and can change only through fluxes across the boundary surface  $S$  (Berger & Field 1984):

$$\frac{d\mathcal{H}}{dt} = 2 \int_S d\mathbf{a} \cdot [(\mathbf{A}_P \cdot \mathbf{B})\mathbf{v} - (\mathbf{A}_P \cdot \mathbf{v})\mathbf{B}], \quad (2)$$

where  $d\mathbf{a}$  points into  $V$ .

The overall budget of coronal helicity has significance for several aspects of solar magnetism. Helicity can serve as a proxy for free magnetic energy (energy above that of the potential field), so a net helicity flux is a proxy for heating. Strict helicity conservation poses an obstacle to several dynamo models (Boozer 1999), which might be removed if helicity were to escape into the heliosphere. Finally, both remote and in situ observations (Zirker et al. 1997; Smith

1999) indicate that the coronal and heliospheric fields in each hemisphere have net helicity, implying some helicity flux through the photosphere.

Several efforts have recently been made to predict theoretically and to quantify observationally the photospheric helicity flux in active region fields. DeVore’s (2000) theoretical work indicates that the helicity flux from differential rotation advecting a passive active region (with unsigned flux  $2\Phi$ ) depends on orientation, peaking at  $d\mathcal{H}/dt \simeq 0.003\Phi^2 \text{ day}^{-1}$  when tilted  $30^\circ$  from east-west. Observational studies show this to be far too low to account for the helicity flux into the heliosphere (Démoulin et al. 2002b; Green et al. 2002; Nindos & Zhang 2002). Furthermore, direct measurements of  $d\mathcal{H}/dt$  using expression (2) differ markedly in sign, magnitude, and time history from the hypothesized passive advection by differential rotation (Chae 2001; Kusano et al. 2002).

While active regions are the most obvious surface fields, they are unevenly distributed over the Sun and vary periodically according to the solar cycle. If the total helicity flux had similar variations, there would be implications for each hemisphere’s overall helicity budget. The full extent to which the helicity budget varies, however, depends on other avenues of helicity flux, most notably the flux through the quiet-Sun magnetic field. The present work is the first to quantify the helicity flux through the quiet Sun.

The quiet Sun’s photospheric field consists of numerous small ( $\Phi \sim 3 \times 10^{18} \text{ Mx}$ ; Schrijver et al. 1997) magnetic elements of mixed polarity, generally found along the network of supergranule boundaries. With  $\sim 10^4$  such elements present at any time, the unsigned flux in quiet-Sun fields is comparable to or greater than that in active regions. Some results (LaBonte & Howard 1982) suggest that the distribution of elements varies little with latitude or solar cycle (at least away from the poles), so it is possible for the quiet Sun to provide a more uniform and constant helicity flux than active regions.

<sup>1</sup> Also at Physics Department, Montana State University, Bozeman, MT 59717-3840.

Section 2 derives the expression for helicity flux through a quiet-Sun field composed of discrete photospheric elements. This is found to consist of a mutual-helicity contribution, due to the interwinding of element pairs, and a self-helicity contribution, due to the internal motions of individual elements. We use this expression to derive a theoretical mutual-helicity flux by assuming a random arrangement of sources moving according to differential rotation. This theoretical estimate is then tested observationally in §§ 3 and 4. Section 3 describes a method of analyzing a sequence of magnetograms to measure the quiet-Sun mutual-helicity flux. This technique is applied to three different data sets from the *Solar and Heliospheric Observatory* Michelson Doppler Imager (*SOHO*/MDI; Scherrer et al. 1995) to calculate the mutual-helicity flux in particular quiet-Sun areas. The results of these measurements are presented in § 4. Section 5 summarizes our results and discusses their implications for the Sun’s overall helicity budget.

## 2. THEORY OF HELICITY TRANSPORT

### 2.1. The Flux of Relative Helicity

We label the two terms in equation (2), from the left, the emergence and braiding terms. The former corresponds to the advection of fields already containing magnetic helicity across the boundary surface, while the latter corresponds to the braiding of footpoints of already-emerged fields that thread the boundary surface.

Recent work by Démoulin et al. (2002a, 2002b) suggests that the dominant source of active region helicity flux into the corona is the inherent twist present in emerging fields. Precisely quantifying the emergence contribution requires knowledge of both the tangential magnetic field and the normal velocity field at the photospheric boundary surface (Kusano et al. 2002). We, however, are primarily concerned with quiet-Sun magnetic fields, in which measurements of the tangential field components are noisy. Furthermore, high-cadence, long-duration data sets are not readily obtainable. For these reasons, we cannot accurately quantify the emergence rate of magnetic helicity in the quiet Sun and neglect its contribution to the total quiet-Sun helicity flux.

Accordingly, we focus solely on the braiding term in equation (2), assuming

$$\frac{d\mathcal{H}}{dt} = -2 \int_S da (A_P \cdot \mathbf{v}) B_z, \quad (3)$$

where we approximate the photosphere as a plane, with  $\hat{\mathbf{z}}$  being the normal vector into the corona.

In the quiet Sun, the photospheric magnetic field is non-zero only in small, isolated regions. The image in Figure 1, the line-of-sight magnetic field as measured by the MDI on *SOHO* in its high-resolution (hi-res) mode (Scherrer et al. 1995), exemplifies this. Consequently, we can accurately approximate the normal magnetic field  $B_z$  at the photosphere as arising from  $N$  pointlike sources.

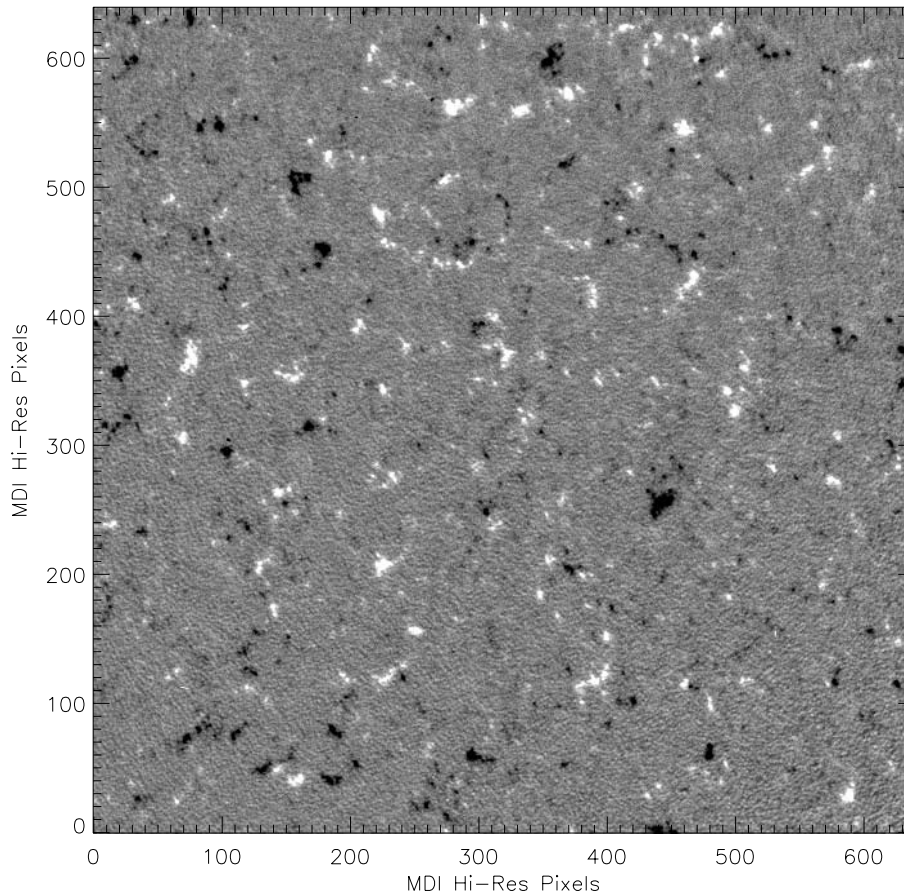


FIG. 1.—First contrast-enhanced, unsmoothed, five-magnetogram average image from data set 1. Each tick mark denotes 10 MDI hi-res ( $0''61$  on a side) pixels. A small active region to the left (east) of this FOV was cropped from the full image.

We define the normalized, flux-weighted average position of the  $i$ th source (its magnetic center of flux) in the usual way:

$$\bar{\mathbf{x}}_i \equiv \frac{1}{\Phi_i} \int_{S_i} da \mathbf{x} B_z(\mathbf{x}), \quad (4)$$

where  $S_i$  is the area covered by the  $i$ th source. Therefore,

$$B_z(\mathbf{x}) = \sum_{i=1}^N \Phi_i \Delta_i(\mathbf{x} - \bar{\mathbf{x}}_i), \quad (5)$$

where  $\Delta_i(\mathbf{x} - \bar{\mathbf{x}}_i)$  is the distribution of flux in the  $i$ th source and is strongly peaked near  $\bar{\mathbf{x}}_i$  and is 0 far away.

In the Coulomb gauge, the vector potential for the current-free magnetic field  $\mathbf{B}_P$ , evaluated on the surface, is then

$$\begin{aligned} \mathbf{A}_P(\mathbf{x}) &= \sum_{i=1}^N \frac{\Phi_i}{2\pi} \int_{S_i} da' \Delta_i(\mathbf{x}' - \bar{\mathbf{x}}_i) \frac{\hat{\mathbf{z}} \times (\mathbf{x} - \mathbf{x}')}{|\mathbf{x} - \mathbf{x}'|^2} \\ &= \sum_{i=1}^N \mathbf{A}_P^{(i)}(\mathbf{x}), \end{aligned} \quad (6)$$

where we have implicitly defined the vector potential due to the  $i$ th flux element,  $\mathbf{A}_P^{(i)}$ . Inserting these expressions into equation (3) and pulling out the  $i = j$  term in the double summation results in an expression for the helicity flux with self and mutual terms (Berger 1999):

$$\begin{aligned} \frac{d\mathcal{H}}{dt} &= -2 \underbrace{\sum_{i=1}^N \Phi_i \int_{S_i} da \left( \mathbf{v} \cdot \mathbf{A}_P^{(i)} \right) \Delta_i(\mathbf{x} - \bar{\mathbf{x}}_i)}_{\text{self}} \\ &+ \underbrace{\left[ -2 \sum_i \sum_{j \neq i} \Phi_j \int_{S_j} da \left( \mathbf{v} \cdot \mathbf{A}_P^{(i)} \right) \Delta_j(\mathbf{x} - \bar{\mathbf{x}}_j) \right]}_{\text{mutual}}. \end{aligned} \quad (7)$$

The self term arises from the braiding of field lines within a single flux element, while the mutual term arises from the braiding of field lines from different flux elements. In this paper, we concern ourselves only with the mutual-helicity flux term. In a subsequent paper, currently in preparation, we build on this derivation to find the self-helicity from non-axisymmetric flux elements, thereby generalizing the helicity flux expression presented in Berger's (1999) review.

## 2.2. Mutual-Helicity Flux

Since  $i \neq j$  by assumption in the mutual-helicity flux term, we are dealing with fluxes in distinct locations, and we can approximate the flux distribution functions  $\Delta_i$  in equation (5) with Dirac  $\delta$ -functions at the locations  $\bar{\mathbf{x}}_i$ . The resulting integrations in each  $\mathbf{A}_P^{(i)}$  are simple and yield circumferential vector potentials for each source, meaning that the full expression for the mutual helicity becomes

$$\frac{d\mathcal{H}}{dt} \simeq -\frac{1}{\pi} \sum_i \sum_{j \neq i} \Phi_i \Phi_j \Omega_{ij}(\mathbf{x}_i, \mathbf{x}_j), \quad (8)$$

where

$$\Omega_{ij}(\mathbf{x}_i, \mathbf{x}_j) \equiv [\mathbf{v}(\bar{\mathbf{x}}_j) - \mathbf{v}(\bar{\mathbf{x}}_i)] \cdot \frac{\hat{\mathbf{z}} \times (\bar{\mathbf{x}}_j - \bar{\mathbf{x}}_i)}{|\bar{\mathbf{x}}_j - \bar{\mathbf{x}}_i|^2} \quad (9)$$

is the angular velocity of the  $j$ th flux element about the  $i$ th. We therefore find the mutual-helicity flux from each pair of fluxes to be

$$\frac{d\mathcal{H}_{ij}}{dt} \equiv -\frac{2}{\pi} \Phi_i \Phi_j \Omega_{ij}, \quad (10)$$

where  $i$  and  $j$  are fixed.

The negative sign means that winding a pair of oppositely signed fluxes in the right-hand sense, with respect to  $\hat{\mathbf{z}}$ , leads to a positive flux of helicity, while right-handed braiding of two fluxes of the same sign causes a negative flux of helicity.

## 2.3. Expected Mutual-Helicity Flux

The photospheric differential rotation systematically winds magnetic fluxes at different latitudes about each other. In the northern hemisphere, for instance, fluxes wind about each other in a right-hand sense, with respect to a radial normal vector. We now make a rough estimate of the average quiet-Sun mutual-helicity flux,  $\langle d\mathcal{H}/dt \rangle$ , from this effect.

Given a distribution of  $2N$  magnetic flux elements,  $N_+$  of flux  $+\Phi_0$  and  $N_-$  of flux  $-\Phi_0$ , with  $N = N_+ = N_-$ , uniformly distributed over a surface area  $A$ , the average spatial probability distribution of fluxes is constant:  $\mathcal{P}_{\pm}(\mathbf{x}) = N/A$ .

The total expectation value of the mutual-helicity flux is the sum of the expectation values from all pairings, each of which is given by an integration over the rotation profile, weighted by  $\mathcal{P}_{\pm}(\mathbf{x})$ . Most terms in the sum cancel, since there are nearly as many homogeneous (+/+ and -/-) pairings ( $2N^2 - 2N$ ) as there are heterogeneous (+/- and -/+) pairings ( $2N^2$ ), and they differ only in sign. Thus, we are left with

$$\left\langle \frac{d\mathcal{H}}{dt} \right\rangle = 2N \left( \frac{\Phi_0^2}{\pi} \right) \frac{1}{A^2} \int dA_i \int dA_j \Omega_{ij}(\mathbf{x}_i, \mathbf{x}_j) = H_0 \bar{\Omega}, \quad (11)$$

where we have implicitly defined a characteristic helicity,  $H_0 = 2N\Phi_0^2/\pi$ , and an average relative rotation rate,  $\bar{\Omega}$ .

Expression (11) depends critically on the *granularity* of the quiet-Sun flux. Since it scales linearly with the number of elements and quadratically with their sizes, the helicity flux vanishes in the nongranular limit  $\Phi_0 \rightarrow 0$ , while  $N\Phi_0 \rightarrow \text{const}$ . This is quite natural, since the positive and negative flux contributions go over, in this limit, to uniform photospheric fields of strength  $B_z^{(\pm)} = \pm\Phi_0 N/A$  and thus cancel each other out; the nongranular limit is a field-free one. Had the two polarities' spatial distributions been unequal, so that  $B_z^{(+)} \neq -B_z^{(-)}$ , the nongranular limit would have yielded a net helicity flux, as in continuum treatments of active regions ( DeVore 2000). Thus, the helicity flux from the quiet Sun's field depends critically on both the sizes and the locations of the discrete elements that compose it.

In accordance with the observations of Schrijver et al. (1997) and this work (see below), we assume a typical flux size of  $\Phi_0 \sim 3 \times 10^{18}$  Mx, giving a characteristic helicity  $H_0/N \sim 10^{37}$  Mx<sup>2</sup> per pair of fluxes.

We estimate  $\bar{\Omega}$  from an expansion of the rotation rate in the vertical position in a plane-parallel approximation to the photosphere in MDI's field of view (FOV). For most of the FOVs in our study (see below), we find  $\bar{\Omega} \sim 3 \times 10^{-7}$  rad s<sup>-1</sup>, using Snodgrass's (1983) rotation rates for the magnetic photosphere.

The expected rate of mutual-helicity flux through the MDI FOV is then  $\langle d\mathcal{H}/dt \rangle_{\text{FOV}} \sim 10^{32} \text{ Mx}^2 \text{ s}^{-1}$ , where we have estimated the number of pairs of flux elements in the FOV to be  $N = 100$ . A typical FOV contains  $\sim 5 \times 10^5$  pixels, each 440 km on a side, meaning that we predict a helicity flux density on the order of

$$\left\langle \frac{d\mathcal{H}}{dt} \right\rangle \sim 10^{11} \text{ Mx}^2 \text{ s}^{-1} \text{ cm}^{-2}. \quad (12)$$

### 3. METHODS

#### 3.1. Data

We analyzed *SOHO*/MDI magnetograms for the photospheric magnetic field  $B_z$  used in our study. The instrument finds the line-of-sight magnetic field by inverting the Stokes  $V$  profile in the Ni I  $\lambda 6768$  line, which is formed at the photosphere (Scherrer et al. 1995). The data sets analyzed were all taken in the instrument's hi-res mode, with  $0''.61$  pixels. At *SOHO*'s position at the L1 point between the Earth and the Sun, this corresponds to about 440 km on the Sun.

We tracked fluxes in five archival magnetogram sequences for 7.5 hr or longer, in regions of predominantly quiet Sun near solar minimum. Three data sets were taken from the same *SOHO* observing campaign; we label these sets 2a, 2b, and 2c. Data sets 1 and 3 were also tracked by Hagenaar et al. (1999), which allows comparison between some of our results and theirs. The observing times, durations, and pointings of the tracking runs are listed in Table 1.

To improve the signal-to-noise ratio in our data, we average five good magnetograms, usually with 1 minute cadence. Occasionally, however, missing or bad magnetograms increase the time between averaged images. We define a bad magnetogram as one in which more than 1000 pixels are either labeled blank or exceed 800 G in absolute value; these are simply skipped over in finding five magnetograms to average. Thus, our measurements of the magnetic field have a nominal time resolution of 5 minutes. The time stamp recorded with the pointing information for each averaged set of magnetograms is the average time of observation for the magnetograms; this avoids timing errors due to data gaps from missing or bad magnetograms. Two small active regions present in data sets 1 and 3 were cropped in the tracked data. (The FOV shown in Fig. 1 is that actually used.)

After averaging, the data are smoothed over  $\sim 3$  pixels by convolution with a potential extrapolation filter. The kernel is the geometrical contribution to the vertical component of the potential field at  $h = 3$  pixels above the photosphere:

$$k(x, y) = \frac{h}{(h^2 + x^2 + y^2)^{3/2}}, \quad (13)$$

assuming the measured fields correspond to point monopoles located at the pixel centers.

To estimate the noise in the measurements, we construct a histogram of the field strengths from the smoothed data. We then fit the core region ( $\pm 2$  G from 0) with a Gaussian, under the assumption that the signal in the core arises entirely from random error. We take the error per pixel for all pixels to be the fitted  $\sigma_n$ ; values of  $\sigma_n$  for the data sets are given in Table 1.

An imbalance in the distribution of field strengths displaces the centroid,  $B_0$ , of the fit from zero. Following Hagenaar et al. (1999), we shift the data in all pixels by  $-B_0$ . In all cases studied, the magnitude of the shift was below the noise, and in most cases, the shift was around 1/10 of the noise level.

#### 3.2. Labeling and Tracking

Having smoothed the data and estimated the error per pixel, we then used a novel, single-pass ‘‘flux-ranked uphill gradient’’ algorithm to group and label pixels into flux elements, which we define to be convex groupings of 10 or more unipolar, contiguous pixels with field strength greater than 10 G in absolute value.

In outline, the algorithm does the following:

1. Ranks pixels' field strengths' absolute values from highest to lowest, down to the 10 G threshold, and labels each pixel with its rank.
2. Proceeds from the highest to the lowest label, at each step comparing the field strengths of each pixel with its eight nearest neighbors and determining which of those nine pixels has the strongest field.
3. Gives the central pixel the label of that pixel with the highest field strength.

Hagenaar et al. (1999) used object selection criteria very similar to ours but with the added constraint that the peak field strength  $B_{\text{max}}$  in each flux element had to exceed 30 G. We found similar flux element densities,  $\rho_{\Phi} \sim (2.5\text{--}3) \times 10^{-9} \text{ km}^{-2}$ , and similar exponential distributions for the

TABLE 1  
DATA SET PARAMETERS

DATA SET	START DATE/TIME (hr:minute)	STEPS TRACKED <sup>a</sup>	SIZE <sup>b</sup> ( $0''.61$ pixels)	POINTING <sup>c</sup>		CARRINGTON ROTATION <sup>d</sup>	$\sigma_n^d$ (G)	$B_0^d$ (G)
				Latitude (deg)	Longitude (deg)			
1.....	1996 Aug 15, 06:22	180	640 $\times$ 640	21.0	8.2	1912.7480	1.65	-0.130
2a.....	1996 Oct 17, 16:05	250	500 $\times$ 1024	12.9	-8.6	1915.0578	1.60	-0.193
2b.....	1996 Oct 18, 21:25	300	500 $\times$ 1024	12.8	7.3	1915.0945	1.62	-0.280
2c.....	1996 Oct 20, 08:51	180	500 $\times$ 1024	12.6	7.9	1915.1678	1.65	0.034
3.....	1997 Jan 16, 22:33	90	1024 $\times$ 250	1.44	0.6	1918.3942	1.52	0.063

<sup>a</sup> Nominal 5 minute step cadence.

<sup>b</sup> Horizontal  $\times$  vertical.

<sup>c</sup> Heliocentric latitude and longitude at the start of the tracking sequence.

<sup>d</sup> At the start of the tracking sequence.

elements' total fluxes,  $f(\Phi_0) \propto \exp(-\Phi/\Phi_0)$ , over a limited range of flux values. Our fitted values for  $\Phi_0$  were in the range of  $(2.8\text{--}3.6) \times 10^{18}$  Mx. In addition, we also found exponential distributions for the flux elements' sizes and average and maximum field strengths.

The flux elements defined by the labeling algorithm described above have been tracked from one five-magnetogram average to the next. Following Hagenaar et al. (1999), we adopt *overlap* as the basic rule for associating flux elements from different time steps. Since differing assumptions in tracking algorithms can lead to differing results, we discuss our algorithm in detail in the Appendix.

To verify that the tracking algorithm works as expected, we plot the tracked rotational and meridional velocities for each data set in Figure 2. The latitudinal variation in our fluxes' sidereal rotation speeds is similar to that in the published differential rotation profile of Snodgrass (1983), obtained by correlation-averaging daily full-disk magnetograms from Mount Wilson. The average and median meridional speeds, at a few meters per second northward, are of the same order of magnitude as published values for meridional motions of sunspots (Howard & Krishnamurti 1986) but are well below the published flow rates of tens of meters per second inferred from helioseismology (González Hernández et al. 1999).

### 3.3. Finding the Mutual-Helicity Flux

We use equation (10) to find the helicity flux from each pair of fluxes  $a, b$  in the time interval  $\Delta t_{k+1,k}$  between  $t_k$  and  $t_{k+1}$ . Averaged values from  $t_k$  and  $t_{k+1}$  are used for  $\Phi_a$  and

$\Phi_b$ . We find  $\Omega_{ab}$  by calculating the angular separation between the vector  $\mathbf{r}_{ab,k}$  that runs between  $\Phi_a$  and  $\Phi_b$  at time  $t_k$  and the vector  $\mathbf{r}_{ab,k+1}$  that links the two at  $t_{k+1}$  and dividing this angular displacement by  $\Delta t_{k+1,k}$ . Finally, the total helicity flux is found by summing that from all pairs.

## 4. RESULTS

### 4.1. Mutual Helicity

In Table 2 we summarize the statistical properties of the measured fluxes of mutual helicity from the data sets. Values in the first four columns are per FOV. In the first column, we show the unweighted average of the mutual-helicity flux for each set,

$$\left\langle \frac{d\mathcal{H}}{dt} \right\rangle_t = \frac{\sum_{k=1}^{N_t} (d\mathcal{H}_k/dt)}{\sum_{k=1}^{N_t} (1)} = \frac{1}{N_t} \sum_{k=1}^{N_t} \frac{d\mathcal{H}_k}{dt}, \quad (14)$$

and the square root of the variance of the helicity flux,  $s$ . The subscript  $t$  on the angle brackets denotes an average over time: the summation index  $k$  is summed over the number of time steps  $N_t$  in each tracking run.

To account for measurement errors, we also calculate the average mutual-helicity flux for each data set using instrumental weighting,

$$\left\langle \frac{d\mathcal{H}}{dt} \right\rangle_\sigma = \frac{\sum_{k=1}^{N_t} [(d\mathcal{H}_k/dt)/\sigma_k^2]}{\sum_{k=1}^{N_t} (1/\sigma_k^2)}, \quad (15)$$

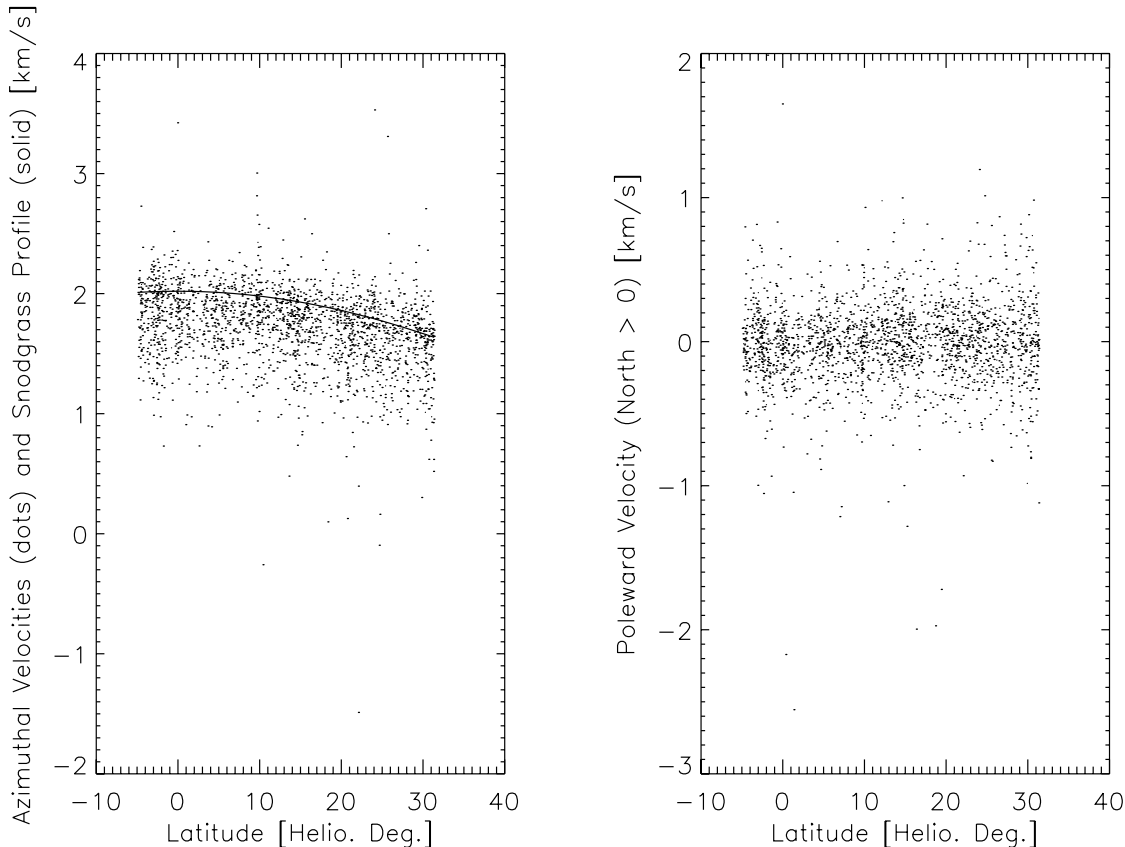


FIG. 2.—Plotted rotational (*left*) and meridional (*right*) velocities as a function of heliographic latitude in data set 2a. The Snodgrass (1983) differential rotation profile is shown in the left panel. Plots for other data sets look similar.

TABLE 2  
MUTUAL-HELICITY FLUXES

Data Set	$\langle d\mathcal{H}/dt \rangle_t \pm s^a$ ( $10^{33} \text{ Mx}^2 \text{ s}^{-1}$ )	$\langle d\mathcal{H}/dt \rangle_\sigma \pm \bar{\sigma}^a$ ( $10^{33} \text{ Mx}^2 \text{ s}^{-1}$ )	Median $(d\mathcal{H}/dt)^a$ ( $10^{33} \text{ Mx}^2 \text{ s}^{-1}$ )	$\langle d\mathcal{H}/dt \rangle \pm \sigma$ ( $10^{13} \text{ Mx}^2 \text{ cm}^{-2} \text{ s}^{-1}$ )
1.....	$-0.443 \pm 80.63$	$-0.0187 \pm 4.29$	-6.85	$-0.00234 \pm 0.537$
2a.....	$-10.2 \pm 328$	$-3.26 \pm 5.34$	6.39	$-0.326 \pm 0.532$
2b.....	$-41.7 \pm 313$	$-16.1 \pm 4.79$	-2.75	$-1.61 \pm 0.479$
2c.....	$-93.5 \pm 590$	$-116 \pm 13.5$	-86.2	$-11.6 \pm 1.35$
3.....	$-9.78 \pm 48.0$	$-5.92 \pm 1.99$	-6.09	$-1.18 \pm 0.398$

<sup>a</sup> Integrated over FOV.

and its average error,

$$\frac{1}{\bar{\sigma}^2} = \sum_{k=1}^{N_t} \frac{1}{\sigma_k^2}, \quad (16)$$

by weighting with the measured errors, which we denote with the subscript  $\sigma$  on the angle brackets. The errors were computed by differentiating our expression for the helicity flux with respect to the measured magnetic fluxes, multiplying by the errors in the magnetic fluxes, and adding the results in quadrature. We estimated the error in magnetic flux for each element using the per pixel noise  $\sigma_n$  (from the final column of Table 1) to be  $\sqrt{N}\sigma_n A$ , where  $N$  is the flux element size in pixels and  $A$  is the area per pixel.

Both methods of finding the average mutual-helicity flux give negative average fluxes in all runs. Both methods also yield relatively small values for data set 1 and relatively large values for data set 2c, which differ from each other by more than 2 orders of magnitude using either method. In most of the data sets, the weighted average values for the mutual-helicity flux are smaller than the unweighted averages. This implies that the errors in the helicity fluxes are larger for larger helicity fluxes, diminishing their contribution to the weighted average.

Both methods of averaging to estimate the mean mutual-helicity flux might be dominated by a few large values of helicity flux of either sign. To check if such a bias is present, we also computed the median value of the helicity flux time series for each tracking run, which is given in the third column of the table. In most cases, the median value is on the same order of magnitude as the averaged values.

To account for the different FOVs in the data sets (see Table 1), we have also calculated the mutual-helicity flux density, and its error, by normalizing the weighted-average helicity flux and its error in each tracking run by the area of the FOV in that run. The results are in the final column of the table.

The table indicates that a typical absolute value of the mutual-helicity flux for an MDI FOV is approximately  $-10^{33} \text{ Mx}^2 \text{ s}^{-1}$ , while a typical flux density is approximately  $-10^{13} \text{ Mx}^2 \text{ cm}^{-2} \text{ s}^{-1}$ .

We plotted the time series of mutual-helicity flux in all five tracking runs in Figure 3; note the differing scales. In each plot of the helicity flux, the solid line is the helicity flux after low-pass filtering. The time series exhibit large fluctuations, but the sets' Fourier transforms share no obvious features.

Most of the error bars are smaller than the excursions of the helicity flux from zero, meaning the measured helicity flux in each data set is not consistent with zero helicity flux. To quantify this, we calculated the value  $\chi^2$  over each data set of  $N_t$  measurements, assuming a zero-flux model, and

computed the value  $P(\chi_{\text{obs}}^2 | N_t)$ , the probability that, given  $N_t$  degrees of freedom, a correct model's  $\chi_{\text{model}}^2$  would be less than  $\chi_{\text{obs}}^2$ . In every data set,  $P(\chi_{\text{obs}}^2 | N_t) = 1$ , implying that the zero-flux model with Gaussian deviations of sizes equal to  $\sigma_k$ , the measurement error at each time step, is ruled out.

A different model in which the data were assumed to be Gaussian excursions of size  $\sigma_k$  about the mean helicity flux  $\langle d\mathcal{H}/dt \rangle_t$  was also ruled out by a similar analysis in every data set.

We conclude that the mutual-helicity flux density in the quiet Sun for our data sets is predominantly negative but intrinsically variable, with an approximate amplitude given by the typical standard deviation in the helicity flux density,  $\sim 5 \times 10^{12} \text{ Mx}^2 \text{ cm}^{-2} \text{ s}^{-1}$ .

#### 4.2. Contributions to Helicity Flux

In § 2.3 we predicted that the mutual-helicity flux would be greater than zero. In every data set, however, we found the flux to be negative. To understand our results, we investigated the contributions of the relative angular velocities of the flux elements and their fluxes to the total mutual-helicity flux given by equation (8).

We expected, from the differential rotation profile in the mostly northern latitudes of our data sets, that the average sense of relative rotation between flux elements would be right-handed. To check this, we binned the flux elements by latitude, computed the average angular rotation of other fluxes about each flux in each time step, and plotted the average value in each bin for each data set. An example plot is shown in Figure 4a. Only in data set 3 is the average of the angular velocities not positive, probably because the differential rotation acts weakly at the low latitudes of its coverage. Hence, we conclude that, as predicted, flux elements rotate about each other in a predominantly positive sense.

Since the measured angular velocities are quite small, but some of the flux elements contain relatively large amounts of flux, we also considered the possibility that the mutual-helicity flux signal was dominated by small, random relative motions in pairings of large fluxes. To investigate this, we calculated the mutual-helicity contributions attributable to a single element  $i$ , due to the motions of all other elements. Plots of this contribution as a function of  $\Phi_i$ , such as the example in Figure 4b, show that the largest contribution to the total helicity comes from the smallest fluxes, which comprise the majority of the population. Evidently, the total mutual-helicity flux distribution was not dominated by the relatively few high-flux elements.

The discrepancy between our predicted and measured flux rates probably arises from our assumption that  $N_+ = N_-$  in our theoretical calculation. If we relax this assumption and repeat the analysis that led to equation (11), we find

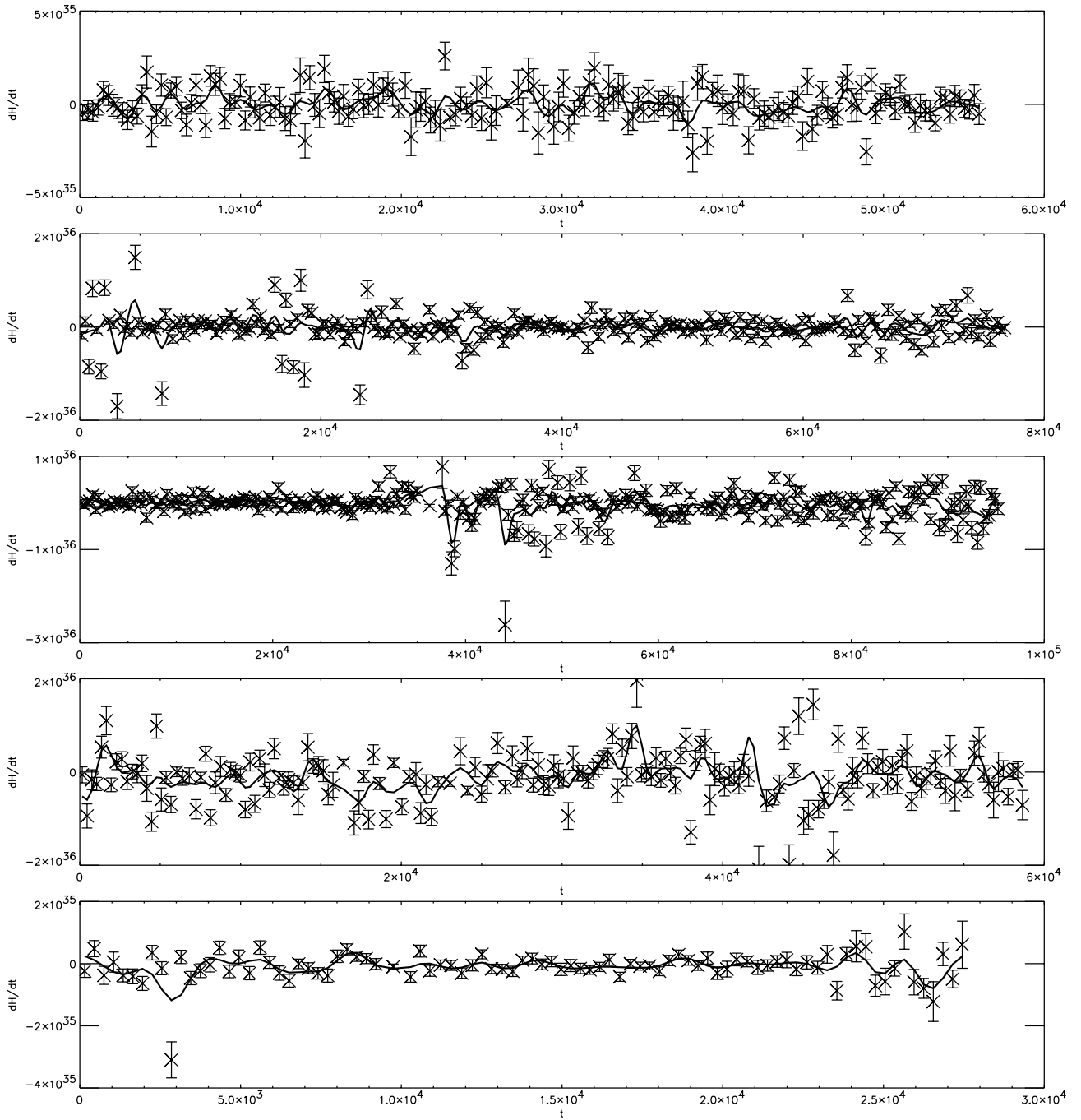


FIG. 3.—Mutual-helicity flux as a function of time in data sets 1, 2a, 2b, 2c, and 3 (top to bottom). Abscissae are in seconds, and ordinates are in  $\text{Mx}^2 \text{s}^{-1}$ . Note the differing scales. Solid lines result from smoothing the time series.

that the coefficient  $H_0$  becomes

$$H_0 = \frac{2\Phi_0^2 [N - (\Delta N)^2/2]}{\pi}, \quad (17)$$

where  $N = (N_+ + N_-)/2$  and  $\Delta N = (N_+ - N_-)$ . Hence, for  $|\Delta N| \geq (2N)^{1/2}$ , the sign of  $H_0$  flips.

In fact, the tracked polarities' imbalance in both number and flux in the first five-magnetogram average in every data set is great enough to explain the sign discrepancy. In sets 1, 2a, 2b, 2c, and 3, the population imbalances  $\Delta N$  for the tracked fluxes were 27, -26, -53, 104, and 37, respectively,

while the rounded values of  $(2N)^{1/2}$  were 19, 22, 23, 24, and 15. In addition, the flux imbalances, divided into units of our characteristic quantum of flux,  $\Phi_0 = 3 \times 10^{18} \text{ Mx}$ , corresponded to 39, -66, -69, 237, and 35 of these flux units, respectively. We note that data set 2c had both the largest flux imbalance and the most negative helicity flux rate (see Table 2), in accordance with the quadratic dependence on  $\Delta N$  in equation (17).

We hypothesize that  $\Delta N$  would vanish in a summation over all quiet-Sun fluxes in the northern hemisphere, which, combined with the observed right-handed relative rotation there, would yield a positive flux of helicity.

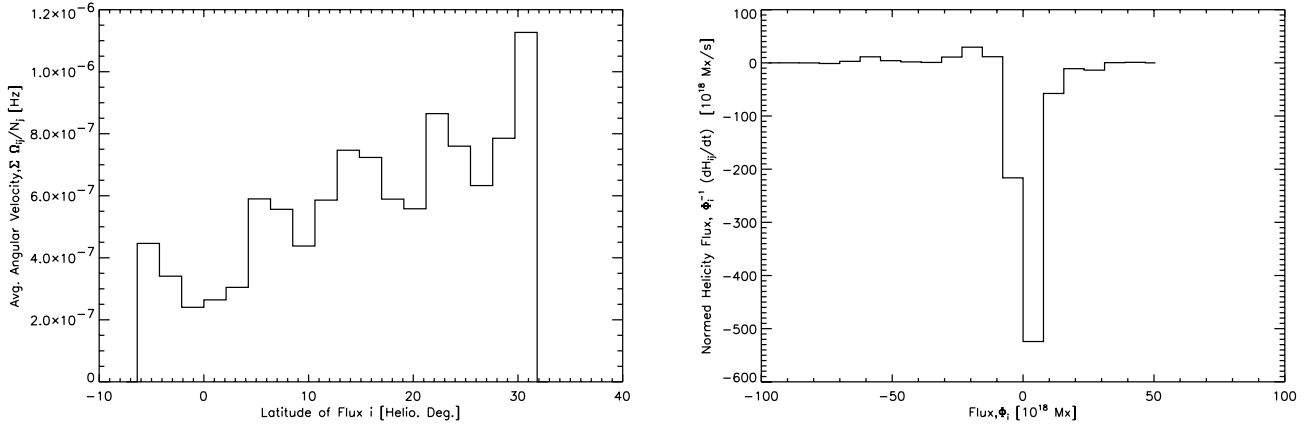


FIG. 4.—(a) Average rotation rate of all other elements about each element, averaged in latitude bins, showing that the sense of relative rotation in data set 2b is positive. (b) Normalized mutual-helicity contribution from each element  $i$ , due to the motions of all other elements, as a function of  $\Phi_i$ , confirming that most of the mutual helicity in data set 2b arises from the smallest fluxes, which comprise a majority of the population.

## 5. CONCLUSIONS

The quiet-Sun mutual-helicity flux fluctuates rapidly, but in a manner inconsistent with Gaussian measurement deviations about a mean mutual-helicity flux rate equal either to zero or to the average flux rate in each tracking run. From the flux imbalances present in all data sets, the average mutual-helicity flux in all sets is negative and on the order of approximately  $-5 \times 10^{12} \text{ Mx}^2 \text{ cm}^{-2} \text{ s}^{-1}$ , although fluctuations ranged almost 3 orders of magnitude higher in amplitude. Our prediction for the average mutual-helicity flux was in the range of  $10^{11} \text{ Mx}^2 \text{ cm}^{-2} \text{ s}^{-1}$ , opposite in sign and roughly an order of magnitude smaller than the observed average flux rates in the data set.

The temporal coverage of our data sets is limited and falls near the minimum of the solar cycle. Nonetheless, we can make an order-of-magnitude estimate of the absolute value of the whole-cycle, quiet-Sun flux of mutual helicity from our results. Multiplying our unsigned helicity flux density by the length of a cycle gives

$$\mathcal{H}_{\text{cyc}} \sim 10^{21} \text{ Mx}^2 \text{ cm}^{-2} \quad (18)$$

through the lower latitudes ( $<30^\circ$  heliocentric) of the northern hemisphere over an 11 yr cycle.

With the caveat that the cycle-dependent concentration of weak unipolar flux at the Sun's poles might cause the actual absolute helicity flux density to increase greatly toward the poles (as the flux imbalance increases), we can extrapolate our results to include the polar regions, which gives a whole-cycle helicity flux of

$$\mathcal{H}_{\text{cyc}}^{(\text{NH})} \sim 10^{43} \text{ Mx}^2 \quad (19)$$

through the northern hemisphere.

Published estimates of the flux of helicity from active regions (Démoulin et al. 2002b; Green et al. 2002; DeVore 2000) suggest that  $\sim 10^{43} \text{ Mx}^2$  of helicity (or more) can come from a single active region. Hence, the contribution to the

Sun's total helicity budget from the braiding of quiet-Sun fluxes is negligible compared to the contribution from active region fields, assuming  $\sim 10^3$  active regions emerge per cycle.

While the cycle-integrated magnetic fluxes in quiet-Sun fields and active region fields are commensurate (both near  $\sim 10^{25} \text{ Mx}$ ), DeVore's (2000) cycle-integrated active region helicity flux from differential rotation is 3 orders of magnitude larger than the comparable quiet-Sun helicity flux we derived. This difference arises from the fine mixture of the quiet Sun's fluxes, which implies that the helicity flux must depend on its granularity. This dependence is in contrast to that of active regions, whose flux distribution is structured on a particular scale that defines its helicity injection rate, independent of its smallest scale properties.

However, we have not considered all the terms in the full expression for the quiet-Sun helicity flux here. In another paper, currently in preparation, we present measurements of the quiet-Sun self-helicity flux rate from braiding motions, and the emergence of quiet-Sun fields already containing helicity through the photosphere, which we neglected when we dropped the left term of equation (2), might make a significant contribution to the Sun's helicity budget. We note that the high spatial resolution, high-cadence, long-duration observations of the quiet-Sun vector magnetic field that should be possible with the focal plane package on the *Solar-B* mission (now scheduled for launch in 2005) might allow a quantitative estimation of the quiet-Sun helicity emergence rate.

The authors acknowledge the anonymous referee, whose comments led to an improved manuscript. This work was supported in part by NSF grant ATM 97-33424, in part by NASA grant NAG5-6110, and in part by the Institute for Theoretical Physics, which is supported by NSF grant PHY 99-07949. We thank the American public for its generous support of these agencies and, ultimately, our work.

## APPENDIX

## TRACKING ALGORITHM

For two fluxes to overlap in our tracking algorithm, the centers of flux of two elements, labeled  $a$  and  $b$ , at times  $t_k$  and  $t_{k+1}$ , respectively, must lie within  $r_{\text{size}}$  pixels of each other, where

$$r_{\text{size}} \equiv \sqrt{\max(\text{size}(a), \text{size}(b))}. \quad (\text{A1})$$

In words,  $r_{\text{size}}$  is the square root of the area of the flux element of the greatest size, in pixels. This approach is ideally suited for high-cadence measurements of features of finite extent but is not suited to low-cadence data sets or to tracking pointlike features, e.g., G-band bright points.

To search for matches between flux elements at time  $t_k$  and fluxes from an adjacent time  $t_l$ , with  $l = k \pm 1$ , the first algorithm we use finds the five nearest neighbor fluxes at  $t_l$  for every flux at  $t_k$  and determines which overlap. The procedure is then repeated with the roles reversed.

The next routine sorts through the nearest neighbor arrays to determine each flux's relation to the fluxes in the adjacent time step. In terms of fluxes from these old and new sets, there are only five possibilities:

1. Disappearance of an old flux.
2. Appearance of a new flux.
3. One-to-one matches between one old and one new flux.
4. Collisions of old fluxes to produce one new flux.
5. Fragmentations of one old flux to produce new fluxes.

We note that collisions and fragmentations always involve fluxes of the same sign.

A flux from an earlier time step that has no overlapping counterpart in a later time step is labeled as a “disappearance.” An “appearance” occurs in an analogous fashion, when a flux from a later time step has no overlapping counterpart in an earlier one.

Ideally, each instance of the disappearance/appearance of flux of a given sign could be matched with an equivalent change of flux of the opposite sign, as a natural consequence of the divergence-free nature of magnetic fields. In practice, however, our tracking method can lead to ambiguities in interpreting the appearance or disappearance of flux: field strengths could randomly decrease below our 10 G threshold (by turbulent diffusivity, for instance), and flux elements could wander in and out of the FOV. Hence, there is not always an obvious physical interpretation to the disappearance/appearance of a labeled flux element in our data sets.

Flux elements that *mutually* overlap are candidates for some type of matching: one-to-one, collision, or fragmentation. In relatively empty regions where flux elements are widely separated, fluxes may have only one overlap and may be each other's nearest neighbors; if so, they are obviously a one-to-one match. After finding the submergences and emergences described above, the matching algorithm looks for just such clear-cut cases of one-to-one matches. In crowded regions, where many fluxes may overlap, the matching algorithm still pairs mutual nearest neighbors as one-to-one. Other fluxes that remain unmatched after a first pass are then checked again. If they mutually overlap and are both unmatched, but one is not the other's nearest neighbor, they are still matched one-to-one.

Flux elements still not matched but that *do* mutually overlap with some already-matched flux element from the adjacent time step are labeled either a collision or a fragmentation. A collision occurs when two or more flux elements from the old time step overlap one from the new time. The sizes of the parent fluxes are compared, and the child takes the label of the larger parent. A fragmentation occurs with the roles reversed: two or more new flux elements overlap one old flux, and the larger child takes the parent's label.

The processes described above must satisfy equations of detailed balance in each step of the tracking. These equations relate the numbers of flux elements at the new and old time steps ( $N_{\text{new}}$  and  $N_{\text{old}}$ , respectively) to the numbers propagated ( $N_{\text{oto}}$ ), created ( $N_{\text{app}} + N_{\text{frag}}$ ), and destroyed ( $N_{\text{disapp}} + N_{\text{coll}}$ ):

$$N_{\text{new}} = N_{\text{old}} + N_{\text{app}} + N_{\text{frag}} - N_{\text{disapp}} - N_{\text{coll}}, \quad (\text{A2})$$

$$N_{\text{new}} = N_{\text{oto}} + N_{\text{app}} + N_{\text{frag}}, \quad (\text{A3})$$

$$N_{\text{old}} = N_{\text{oto}} + N_{\text{disapp}} + N_{\text{coll}}. \quad (\text{A4})$$

The tracking routine stops with an error flag if any of these constraints are violated at any tracking step. In practice, about 90% of flux elements are matched one-to-one in each tracking step.

Statistics on appearance, disappearance, collision, and fragmentation rates were compiled. Our collision and fragmentation rates were higher than those of Hagenaar et al. (1999), which is probably a result of differing definitions of collisions and fragmentations in our tracking algorithms.

## REFERENCES

- Berger, M. A. 1999, in *Magnetic Helicity in Space and Laboratory Plasmas*, ed. M. R. Brown, R. C. Canfield, & A. A. Pevtsov (Geophys. Monogr. 111; Washington, DC: AGU), 1
- Berger, M. A., & Field, G. B. 1984, *J. Fluid Mech.*, 147, 133
- Boozer, A. H. 1999, in *Magnetic Helicity in Space and Laboratory Plasmas*, ed. M. R. Brown, R. C. Canfield, & A. A. Pevtsov (Geophys. Monogr. 111; Washington, DC: AGU), 11
- Chae, J. 2001, *ApJ*, 560, L95

- Démoulin, P., Mandrini, C. H., van Driel-Gesztelyi, L., López Fuentes, M. C., & Aulanier, G. 2002a, *Sol. Phys.*, 207, 87
- Démoulin, P., Mandrini, C. H., van Driel-Gesztelyi, L., Thompson, B. J., Plunkett, S., Kóvári, Z., Aulanier, G., & Young, A. 2002b, *A&A*, 382, 650
- DeVore, C. R. 2000, *ApJ*, 539, 944
- Finn, J. M., & Antonsen, T. M., Jr. 1985, *Comments Plasma Phys. Controlled Fusion*, 9, 111
- González Hernández, I., Patrón, J., Bogart, R. S., & The SOI Ring Diagram Team 1999, *ApJ*, 510, L153
- Green, L. M., López Fuentes, M. C., Mandrini, C. H., Démoulin, P., van Driel-Gesztelyi, L., & Culhane, J. L. 2002, *Sol. Phys.*, 208, 43
- Hagenaar, H., Schrijver, C., Title, A., & Shine, R. 1999, *ApJ*, 511, 932
- Howard, L. H., & Krishnamurti, R. 1986, *J. Fluid Mech.*, 170, 385
- Kusano, K., Maeshiro, T., Yokoyama, T., & Sakurai, T. 2002, *ApJ*, 577, 501
- LaBonte, B. J., & Howard, R. 1982, *Sol. Phys.*, 80, 15
- Nindos, A., & Zhang, H. 2002, *ApJ*, 573, L133
- Rust, D. 2002, in *Proc. 2d Solar Cycle and Space Weather Euroconference*, ed. H. Sawaya-Lacoste (ESA SP-477; Noordwijk: ESA), 39
- Scherrer, P., et al. 1995, *Sol. Phys.*, 162, 129
- Schrijver, C. J., Title, A. M., van Ballegoijen, A. A., Hagenaar, H. J., & Shine, R. A. 1997, *ApJ*, 487, 424
- Smith, C. W. 1999, in *Magnetic Helicity in Space and Laboratory Plasmas*, ed. M. R. Brown, R. C. Canfield, & A. A. Pevtsov (Geophys. Monogr. 111; Washington, DC: AGU), 239
- Snodgrass, H. 1983, *ApJ*, 270, 288
- Taylor, J. B. 1974, *Phys. Rev. Lett.*, 33, 1139
- Zirker, J. B., Martin, S. F., Harvey, K. H., & Gaizauskas, V. 1997, *Sol. Phys.*, 175, 27